2019-24-0075

Performance and emissions of an advanced multi-cylinder SI engine operating in ultra-lean conditions

F. Bozza, D. Tufano, E. Malfi, L. Teodosio, V. De Bellis – University of Naples Federico II
C. Libert – Renault SA

Abstract

In this work the performance and noxious emissions of a prototype Spark Ignition (SI) engine, working in ultra-lean conditions, are investigated. It is a four-cylinder engine, having a very high compression ratio, and an active pre-chamber. The required amount of air is provided by a low-pressure variable geometry turbocharger, coupled to a high-pressure E-compressor. The engine is equipped with a variable valve timing device on the intake camshaft.

The goal of this activity is to support the development and the calibration of the described engine, and to exploit the full potential of the ultra-lean concept. To this aim, a combustion model for a pre-chamber engine, set up and validated in a previous paper for a similar single-cylinder unit, is utilized. It is coupled to additional in-house developed sub-models, employed for the prediction of the in-cylinder turbulence, heat transfer, knock and pollutant emissions.

Such a complex architecture, schematized in a commercial 1D modeling framework, presents several control parameters which have to be properly selected to maximize the engine efficiency and minimize the noxious emissions over its whole operating domain.

A Rule-Based (RB) calibration strategy is hence implemented in 1D model to identify the optimal values of each control variable. The reliability of the RB calibration is also demonstrated through the comparison with the outcomes of a general-purpose optimizer, over a load sweep at a constant speed.

The 1D model and the RB methodology are then applied for the performance prediction over the whole engine operating domain. The predicted performances show the possibility to achieve a wide zone of very high efficiency, with limited penalizations only at very low loads. Main advantages of the lean-combustion concept are highlighted, concerning reduced heat losses, improved knock mitigation, and abatement of pollutant emissions, especially regarding CO and NO.

The presented methodology demonstrates to be a valuable tool to support the development and calibration of the considered high-efficiency engine architecture.

Introduction

The debate about how to face the impact of Internal Combustion Engines (ICEs) on atmospheric air pollution and climate changes is still open [1,2]. Some studies [3] foresee the complete disappearance in few years of the ICE-based propulsion systems in the automotive sector, replaced by fuel cell and/or Battery Electric Vehicles (BEVs). Other analyses consider additional issues, mainly regarding the customers' expectations, the electricity management and BEVs operating limitations [4,5]. In the light of those concerns, a smoother and longer transition from ICEs to the above-mentioned solutions is really expected. In the medium-term, indeed, Hybrid Electric Vehicles (HEVs) are certainly the most suitable options, since the hybridization allows to overcome the major disadvantages of ICEs and electric units, merging the related benefits. In this scenario, the ICEs are expected to remain the core component of automotive propulsion systems in the years to come. Nevertheless, a further effort for the improvement of the efficiency and pollutant emissions of the ICEs is mandatory. HEVs equipped with high-efficiency ICEs are the most promising path to respect the more and more stringent fleet limits on CO_2 emission [6].

Concerning Spark Ignition (SI) ICEs, widespread methods for efficiency improvement have been investigated during last decade, including Variable Valve actuation and/or Timing (VVT) systems, downsizing coupled to turbocharging, variable compression ratio [7], water injection and external cooled Exhaust Gas Recirculation (EGR). The benefit obtained by all of those technologies highly depends on the operating condition where the engine works. At very low load/speed, most frequently covered by the engine during WLTC driving cycle, the fuel consumption advantage is rather limited [8]. In addition, each of the above recalled solutions causes an increase of the engine complexity and cost. In the case of a HEV, the ICE usually works in the med/high load region, and the above concerns at reduced loads are less felt.

Since many years, it is very well known that a further improvement of the engine efficiency can be obtained working with lean air/fuel mixtures. The better efficiency mainly derives from reduced heat losses and higher knock resistance, as shown in [9]. Additionally, this path ensures a consistent decrease of NOx emissions and the practical absence of CO and HC emissions [10]. For a conventional SI ICE, however, the allowed excess-air is rather limited, due to the mixture ignitability and combustion stability. A lean combustion results in a slower burning speed, leading to unacceptable cyclic variability, misfire and HC / CO formation increments [11,12]. In addition, in

lean operation, the common three-way catalyst highly loses its abatement efficiency.

Compared to a conventional SI engine, the employment of a Pre-Chamber (PC), characterized by a small volume (usually 1%-5% of the total combustion chamber volume) and connected with the Main-Chamber (MC) through one or more orifices, can significantly extend the lean burn limit [13,14]. In such a system, the combustion process starts at the spark plug located in the pre-chamber. Because of the heat released by the PC combustion, multiple turbulent jets of hot gas are ejected from the pre-chamber. These jets penetrate the main-chamber, increasing the turbulence, and igniting the lean mixture along each of them. As a consequence, the burn rate enhances, improving the combustion stability even for extremely lean mixtures.

Various experimental activities have been reported in the current literature, showing the benefits of an active pre-chamber in reducing the NO_X emissions, extending the lean limit and improving the thermal efficiency [15,16]. To get better mixture formation in an active pre-chamber, gaseous fuels, such as ethanol [17] and hydrogen [18], or vaporized gasoline [19] have been investigated. However, considering the fuel supply infrastructure for passenger cars, the liquid gasoline injection into the pre-chamber remains the most suitable option, although some risk of a not-perfect mixture formation may arise.

The introduction of a PC instead of a conventional ignition system enhances even more the complexity of a modern SI engine architecture, also considering the increased degrees of freedom for the engine calibration. One of the most demanding tasks is in this case a reliable control of the air/fuel mixture quality, especially in the PC, where a certain inhomogeneity is expected to occur. In addition, the control of a two-stage turbocharging system is usually required to provide the correct amount of excess-air in each operating condition [20].

The ultra-lean combustion concept is also the focus of a research work supported by a European Union H2020, named EAGLE (https://h2020-eagle.eu/). The project includes integrated experimental and numerical activities aiming to design a thermal unit having a much more reduced fuel consumption and CO_2 emissions compared to a conventional SI engine.

The activities reported in this work were developed within the framework of the above-mentioned project and aim to numerically investigate the potential of this novel engine architecture. To support the design and the calibration phases, a predictive quasi-dimensional combustion model for a pre-chamber engine has been previously developed and validated in a prototype single-cylinder unit [21]. The same model is applied in this work to foresee the complete multi-cylinder engine performance maps. The study is developed in a 1D modeling framework, where the other in-cylinder phenomena, such as turbulence, knock and heat transfer are described by refined sub-models developed by the authors.

To predict the performance maps, a Rule-Based (RB) calibration strategy is set up, aiming to maximize the engine efficiency over the whole engine operating domain. To verify the reliability of the RB calibration approach, a cross-numerical validation with a calibration procedure employing an external optimizer is carried out.

The paper is organized as follow: firstly, the main characteristics of the ultra-lean engine are described. Then, the essential features of the turbulent combustion model are briefly recalled. Subsequently, the numerical RB calibration procedure is described and verified against a more complex approach, implemented in a multi-purpose optimizer. Finally, the RB calibration is employed to compute performance and emissions maps. Predicted performance are discussed to highlight the advantages of the lean-combustion concept, due to reduced heat losses, improved knock mitigation, and reduced of CO and NO emissions. Preliminary analyses, not reported in the paper, let foresee that the developed engine, embedded in a plug-in HEV, will lead to a CO_2 emission of about 50g/km along a WLTC.

Engine Description

The main features of the analyzed engine are listed in Table 1. To better clarify the engine architecture, its layout is schematized in Figure 1. It is a prototype four-cylinder SI engine, equipped with an active pre-chamber ignition system. The PC presents four orifices by which it is connected to the main-chamber. Each cylinder is fitted with two intake and two exhaust valves. The engine presents a VVT device at the intake camshaft, allowing for an advanced closure (Miller concept [22]). Four port fuel injectors, one for each cylinder, supply liquid gasoline, just upstream the intake valves (Inj_{MC}). Liquid gasoline is directly injected into the PC, as well (Inj_{PC}). The engine boosting system is composed of a Low-Pressure Compressor (LPC) connected to a variable geometry Low-Pressure Turbine (LPT) and a High-Pressure (HP) compressor (E-Comp), driven by an Electric Motor (EM). The crankshaft (in blue in Figure 1) moves the Electric Generator (EG) which, in turn, recharges the battery (Ba) and powers the EM. The electric flux is depicted as a red dashed line in Figure 1.

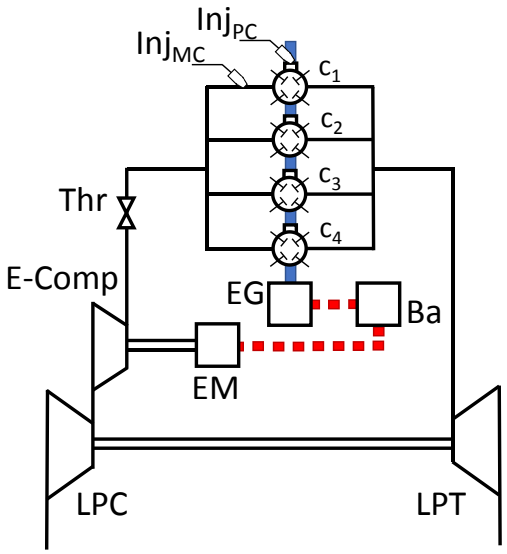

Figure 1. Schematic engine layout.

For such a complex engine architecture, a very challenging control has to be faced. It consists of the selection of the control variables in the whole operating domain minimizing the engine efficiency and complying with proper constraints on some monitored parameters. This engine has seven control parameters, namely the air-fuel mixture quality (here treated in terms of relative air-to-fuel ratio λ) in both pre-chamber and main-chamber (labelled as λ_{PC}, and λ_{MC}, respectively), the rack position of the LPT, the electrical power absorbed by the E-Comp (or equivalently its rotational speed), the intake valve timing, the spark advance and the throttle valve position. The engine is designed to operate at very lean air/fuel mixtures with the aim of improving the engine efficiency and of reducing the nitrogen oxide emissions.

Table 1.Engine main features.

Multi-cylinder pre-chamber engine	
Bore, mm	76
Stroke, mm	90
Displacement, cm^3	1633
Peak pressure limit, bar	180
Geometrical compression ratio	15.8 (including PC volume)
Fuel in main-chamber	PFI injector, gasoline RON 95
Fuel in pre-chamber	DI injector, gasoline RON 95
Pre-chamber volume mm^3	~ 1000
$V_{pre\text{-}chamber}$ / V_{TDC}	~ 3 %
Pre-chamber holes	4 - two pairs of different hole size
$A_{jet\ holes}$ / $V_{pre\text{-}chamber}$, cm^{-1}	~ 0.03
Intake Valve Opening Range (IVO)	3/48 CAD BTDC (@0.2 mm lift)
Exhaust Valve Closure (EVC)	19 CAD ATDC (@0.2 mm lift)
Start of Port Fuel Injection	140 CAD BTDC
Start of Direct Injection inside PC	300 CAD BTDC

1D Engine Model Description

A 1D model of the above described engine is developed within a 0D/1D modelling framework, where the system is schematized through a network of 1D pipes, 0D cylinders and junctions. The operation of the boosting system is reproduced by a standard map-based approach. The flow permeability of the cylinder head is modelled through steady-state flow coefficients, measured on a similar single-cylinder research engine [15]. During PFI and DI injections, 30% of the injected fuel is assumed to instantaneously evaporate, while no advanced treatment of spray evolution and liquid wall film formation are considered. The mechanical friction losses are estimated by an empirical correlation, function of engine speed, combustion phasing and in-cylinder pressure peak. Regarding the schematization of both PC and MC, they are modelled as two 0D volumes, connected through four equally-sized orifices. In particular, the hole diameters are assigned to realize the same overall cross-sectional area as the real holes. A fixed value of the discharge coefficient (0.65) is selected to get a good agreement with the differential PC-MC pressure along the compression stroke. The PC is schematized as constant volume element, connected to a standard variable volume representing the MC. Mass and energy balance equations are solved in both volumes and a filling/emptying method is used to estimate the mass exchange between them, based on pressure difference, overall cross-sectional area and discharge coefficient of the orifice.

The combustion model is based on a two-zone (burned and unburned gases) description. The combustion evolution is described by a re-assessed quasi-dimensional fractal model, developed by the authors in the last years [23]. The model is utilized in a similar way in both MC and PC. According to the fractal theory, the burning rate expression is written as:

$$\frac{dm_b}{dt} = \rho_u A_T S_L = \rho_u A_L S_L \frac{A_T}{A_L} = \rho_u A_L S_L \left(\frac{L_{\max}}{L_{\min}} \right)^{D_3 - 2} \qquad (1)$$

with ρ_u being the unburned gas density, A_L and A_T the area of the laminar and turbulent flame fronts, S_L the laminar flame speed. L_{max} and L_{min} are the length scales of the maximum and minimum flame wrinkling, respectively, and D_3 is the fractal dimension. D_3 is estimated by an empirical correlation as a function of the u'/S_L ratio, u' being the turbulence intensity.

The main hypothesis behind the adopted approach is that the flame front propagates locally at a laminar speed, and that the combustion process is promoted by the turbulence-induced flame wrinkling, the combustion regime falling in the wrinkled corrugated flamelets domain. As widely recognized [24], this is expected to occur in a conventional engine architecture, where the flame front is generated by a spark plug and propagates quasi-spherically. This is also the way in which the combustion is described here within the PC.

Compared to a conventional SI engine, a different description of A_L, S_L, L_{max}, L_{min} and u' is required to properly handle the combustion in the main-chamber. This topic is deeply discussed in a previous authors' work [21]. As known, the combustion process in the MC is initiated by some turbulent jets, produced by the pre-chamber. In the proposed schematization, quasi-spherical flame fronts propagate from "fictious" ignition sites located along each turbulent jet. This assumption is based on the observation that the jets quickly dissipate their initial kinetic energy, leading to the onset of a number of flame fronts with almost fixed centers. During the combustion development, the flame fronts intersect each other, until the entire combustion chamber is filled. Such a description determines a much faster combustion process compared to a standard SI engine.

The computation of the laminar flame area A_L in eq. (1) takes into account the flame-to-flame and flame-to-wall intersections, as described in [21]. In particular, a tabulated approach is followed. Look-up tables for both PC and MC are generated in a preliminary stage, based on a simplified geometrical schematization of these volumes. The tables collect the flame area development as a function of the burned gas volume (or equivalently of the flame radius) and, for the sole MC, of the piston position.

Additional mechanisms are considered at the beginning of the MC combustion, more directly related to the turbulent jets. Indeed, the PC jets are expected to increase the flame wrinkling with an intensity proportional to a characteristic jet velocity scale. Air entrainment within the turbulent jets is included in the model, based on a semi-empirical correlation [25].

For the estimation of the laminar flame speed, S_L in eq. (1), a simulation-derived correlation for a TRF gasoline blend, including 10% in volume of ethanol, is utilized for both PC and MC [26].

For the evaluation of L_{max}, L_{min} and u', an "in-house developed" turbulence sub-model [27], belonging to the *K-k-T* family, is adopted. It describes the energy cascade mechanism from the mean flow kinetic energy, *K*, to the turbulent one, *k*, also taking into account a balance equation for the tumble angular momentum, *T*. The model is applied to both chambers and is extended to describe the turbulence production in the pre-chamber, induced by the incoming flow through the orifices during the compression phase. Similarly, an additional turbulence production is considered in the main-chamber because of the penetrating turbulent jets [21].

A hierarchical 1D/3D approach is used for turbulence tuning, as detailed in [27]. The turbulence model tuning here employed is borrowed from an activity on a single-cylinder research engine [21], whose in-head ports, piston shape and PC geometry are similar to the ones of the considered four-cylinder engine.

The tuning of the described quasi-dimensional combustion model was carried out with reference to the above cited research single cylinder engine [21]. This was realized by a trial-and-error procedure to reproduce, as better as possible, the in-cylinder pressure traces in both PC and MC. A single set of constants was determined for all the tested operating conditions, which were characterized by very different speeds, loads and air/fuel mixture qualities (λ up to 2.4 in the main-chamber). The model tuning is borrowed here and kept

fixed regardless of the operating condition, not being available yet experimental data for the considered four-cylinder engine. However, as stated above, this assumption appears reasonable since the single- and the multi-cylinder engines present very similar geometrical characteristics.

The knock phenomenon is described by the Auto-Ignition (AI) calculation of the air/fuel mixture in the unburned zone. AI computation is carried out by a tabulated approach [28], where the AI table is derived by preliminary auto-ignition chemical kinetics simulations in a homogeneous reactor at constant pressure. To this aim, the kinetic scheme in [26] is employed, including 5 elements, 201 species and 1548 reactions. The scheme is modified with the addition of a skeletal sub-mechanism for toluene oxidation to handle a TRF. The table collects the AI time, τ_{AI}, as a function of pressure, temperature, equivalence ratio, and residual content. In the engine model, the knock event is assumed to occur when the AI integral, expressed by Eq. (2), exceeds a tunable threshold level.

$$\int \frac{dt}{\tau_{AI}} \qquad (2)$$

The model also includes an estimation of the main cylinder-out emissions, namely CO, HC and NO. In order to evaluate the CO and NO productions, a multi-zone schematization of the burned zones in both PC and MC is used. It supposes a temperature stratification, where each burned parcel is assumed to compress/expand adiabatically according to the in-cylinder pressure. Starting from the equilibrium concentrations in each burned parcel, the CO and NO concentrations are computed. For the NO, the historical extended Zeldovich mechanism is applied [29], whereas the CO is computed by a two-step reaction scheme [12]. For the HC modeling, among the different formation mechanisms, namely the adsorption/desorption from the oil layer, wall flame quenching and crevices [30-31], the sole crevices contribution is here considered. In particular, unburned hydrocarbons are assumed to accumulate / be released during the pressure rise/decrease phases in/from an arbitrary assigned constant crevices volume [30]. The temperature in this volume is considered to be the same as the cylinder wall, while the pressure is the one in the cylinder. As soon as unburnt fuel is released from crevices volume, it is assumed to be instantaneously oxidized in the cylinder until an assigned "frozen" temperature is reached. This last represents the temperature below which any additional HC-released oxidation occurs.

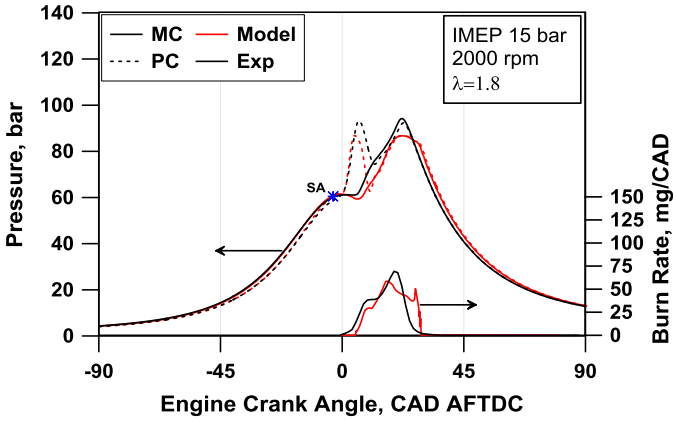

Figure 2. Experimental/numerical comparisons of in-PC and in-MC pressure traces and burn rate at 2000 rpm, 15 bar IMEP, λ_{MC} = 1.8, for the single-cylinder engine in [21].

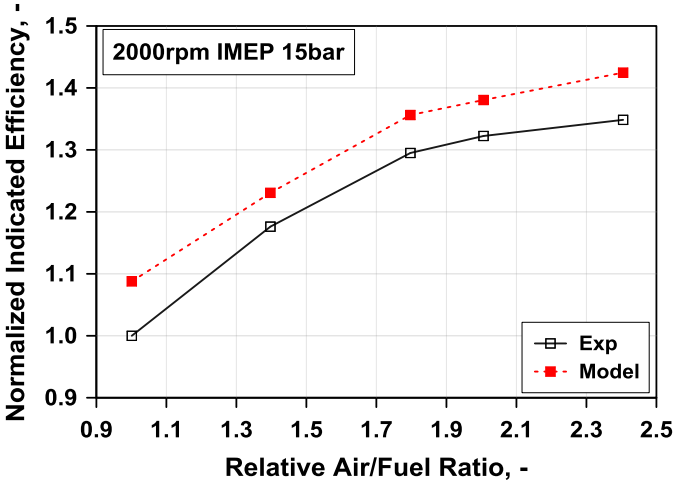

Figure 3 Experimental/numerical normalized indicated thermal efficiency at different λ_{MC} for the single-cylinder engine in [21].

The reliability of the adopted approach has been verified in [21], with reference to a single-cylinder engine. As an example, the experimental/numerical comparisons of the in-PC and in-MC pressure cycles and the related burn rate are shown in Figure 2. The model demonstrated to properly describe the combustion evolution in both chambers, in the selected operating point. A similar accuracy was found for different speeds, loads, and air/fuel mixture qualities. Figure 3 depicts the assessment of the indicated thermal efficiency for various λ_{MC}. The simulation was able to perceive the efficiency improvement at increasing mixture leaning, mainly due to the enhanced knock resistance promoted by the mixture leaning and to the heat losses reduction. A slight systematic model overestimation is probably caused by an underestimation of the heat losses late during the expansion phase.

Rule-Based Approach for Engine Calibration

In order to optimize the engine performance over the whole operating plane, a calibration strategy is here proposed, which is based on a number of heuristic rules. It has to be stressed that the calibration of the considered engine is a very challenging task due to the large number of degrees of freedom available. For this reason, a simplified RB sub-optimal strategy may represent a useful tool to speed up the calibration phase of such an engine. This can lead to a "first attempt" engine mapping, to be refined by a more time-consuming calibration strategy.

The aim of the RB procedure is the maximization of the engine efficiency in each operating point, while complying with several constraints - namely knock intensity, maximum in-MC and in-PC pressure, compressors speed, etc. - required to limit thermal and mechanical stresses of the engine and its subcomponents. The strategy is implemented introducing a network of logical switches, PID controllers and "user routines" in the 0D/1D environment used for the fluid-dynamic simulation. To be more precise, the objective is the maximization of the Overall Brake Thermal Efficiency (OBTE), which is defined as:

$$\mathrm{OBTE} = \frac{P_{ICE} - P_{HPC}/\eta_{HPC}}{\dot{m}_f \,\mathrm{LHV}} \qquad (3)$$

where P_{ICE} is the brake power at the engine shaft, and P_{HPC} is the mechanical power at the E-Comp shaft. η_{HPC} is the electro-

mechanical efficiency of the E-comp, and $\dot{m}_f$ and LHV are the fuel flow rate and the fuel lower heating value, respectively. η_{HPC} takes into account the overall losses in the electric units (EM and EG) and in the battery, while the adiabatic efficiency of the HP compressor is taken into account in the P_{HPC} term. In the following, it was assumed η_{HPC} = 0.81 whatever is the operating condition of the compressor and of the engine. The OBTE definition in Eq. (3) is consistent with a "self-sustaining" engine operation mode, namely, at each time, the engine delivers the power required to sustain the battery for driving the E-Comp. Such a choice can be judged conservative, not taking into account the possibility that the battery charging could be realized under a different operating condition, more convenient from the powertrain management viewpoint along a vehicle driving mission.

The control parameters available for the engine calibration are the spark advance, or alternatively the combustion phasing (MFB_{50}), the mixture qualities in main- and pre-chamber, the rack position for the LPT, the E-Comp speed, the Intake Valve Closure (IVC) timing, and the throttle valve opening. Maximum allowable levels imposed for the constrained parameters are shown below, together with additional limitations:

- Maximum in-PC and in-MC pressures: 180 bar
- Optimal combustion phasing (MFB_{50}): 4.5 CAD AFTDC
- Maximum AI time integral = 0.8
- Injection duration in PC: 300-900 µs
- IVC range: 505 to 540 CAD AFTDC
- Maximum spark advance: -80 CAD AFTDC
- Maximum speed LP group: 205.000
- Maximum speed E-Comp: 140.000

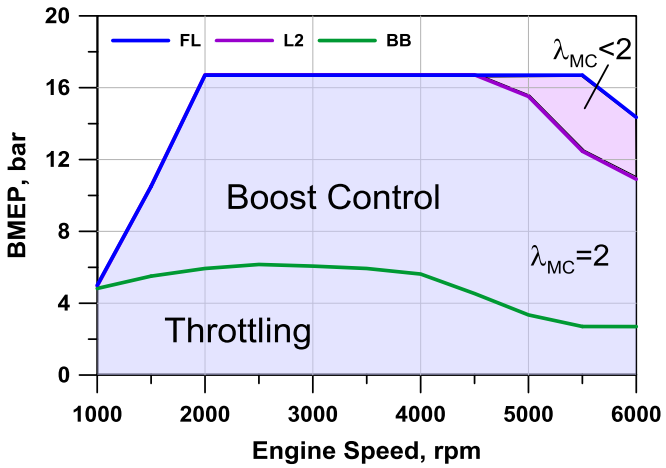

Figure 4. BMEP – rpm plane including the BMEP target (FL), and the L2 and BB lines.

As known, the MFB_{50} realizing the maximum thermodynamic efficiency slightly changes with the operating conditions, and always occurs few crank angles AFTDC. Generally, this value is around 7-10 CAD AFTDC for a conventional SI engine, whereas it is slightly advanced for a PC engine, as shown in [33]. Following the quoted work, a fixed value of 4.5 CAD AFTDC is assigned here. In the proposed strategy, this MFB_{50} target can be realized under knock free operation. Otherwise, the combustion phasing is delayed until the specified threshold level for the knock index is reached. A value of 0.8, hence lower than unity, is specified to preserve a certain knock safety margin. This choice arises since the proposed knock analysis refers to the average cycle, while it is known that "faster-than-average" cycles, due to the cyclic variability, are more likely to knock.

The fuel injected in the pre-chamber is metered to get a stoichiometric level, complying with the above-mentioned limitations on the injection duration. The shortest duration of 300 µs is due to dynamic response of the injector, which does not guarantee a repeatable and reliable operation below such a duration. A λ_{PC} value greater than the unity is specified to limit the in-PC pressure peak below the prescribed limit of 180 bar. The fuel injection in the main chamber is controlled to realize λ_{MC} = 2 over the largest possible operating domain. This setting is modified only at high speed / high load as discussed below.

The strategy to control the LP turbocharger and the E-Comp is differentiated according to the engine load. As a first step, a Full Load (FL) analysis is performed and the FL BMEP target depicted in Figure 4 is assigned. To reach this target, the fuel metering in the MC is firstly controlled to get λ_{MC} = 2 over the whole engine speed range. An arbitrary running line is specified for the LP compressor, reported over the LPC map in Figure 5-top. The LPC running line is chosen as a compromise between an adequate surge margin, and a sufficiently high pressure ratio, to limit the power absorbed by the E-Comp. The E-Comp running line (Figure 5-bottom) is then straightforwardly identified by searching the HP boost level required to match the prescribed FL BMEP target. At very high engine speeds, on the other hand, the E-Comp reaches its maximum rotational speed and the overall pressure ratio is limited. As a consequence, the FL target is not fulfilled above 4500 rpm. Correspondingly, the maximum BMEP level with λ_{MC} = 2 is detected (L2 line in Figure 4). This line defines the upper limit of the operating domain with λ_{MC} = 2 for the considered engine and boost system (highlighted in powder blue in Figure 4). To fulfill the FL target, more fuel has to be injected in the main-chamber, resulting in λ_{MC} < 2 (pink region in Figure 4).

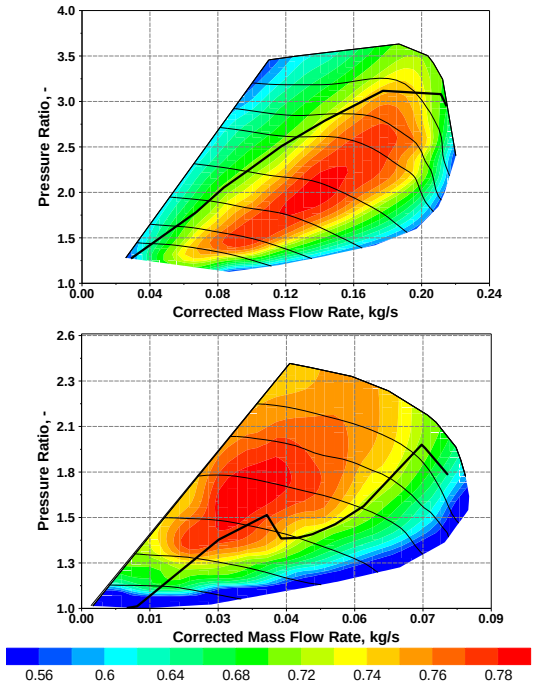

Figure 5. LP (top) and HP (bottom) compressor maps, including the running lines at full load.

The load control is carried out in the high/mid load zone by progressively opening the LPT and reducing the E-Comp speed, starting from the settings identified by the above described steps. While reducing the load, an additional characteristic line over the BMEP-speed plane can be identified, labelled as BB (namely Base

Boost) in Figure 4. This load level is gained when the LPT is fully open and the E-Comp compression ratio is equal to 1. Below this level, the LP and HP compressor settings remain fixed and the load is controlled by progressively closing the throttle valve.

Concerning the intake valve management, generally the IVC is set at the maximum value of 540 CADs AFTDC with the aim of maximizing the cylinder filling and the effective compression ratio. A control strategy is established to exploit the advantages of the intake VVT device under some operating conditions, following the Miller concept. Approximatively, knock limited operation occurs at BMEP levels slightly above the BB line. In these conditions, the IVC is advanced until the computed knock intensity exceeds the prescribed threshold level. In this way, the effective compression ratio is reduced, and the knock is mitigated. If not sufficient to suppress knock, the MFB_{50} is progressively delayed, too. In the region of the map below the BB line, the load is controlled by a concurrent throttle valve closure and IVC advance. In this way, the pumping losses are minimized, and become relevant only at very reduced BMEP levels.

The proposed rule-based approach, although not ensuring to reach the optimal calibration, is sophisticated enough to realize engine operations very close to the minimum BSFC, as demonstrated in the following section. Moreover, it can be implemented in a single control logic block in the adopted 1D software to compute the performance maps much faster than a full multi-objective optimization [34].

Optimization Approach for Engine Calibration

The reliability of the RB engine calibration is verified through the assessment with a more complex methodology. The latter is based on an automatic optimization, implemented in an external multi-purpose optimizer. The aim is the maximization of the overall brake thermal efficiency and the minimization of the Brake Specific Nitric Oxides (BSNO, gNO/kWh). The optimization is performed along a load sweep at a constant engine speed of 3000 rpm. The analysis proposed here regards the rotational speed where the maximum OBTE is expected to occur for the examined engine.

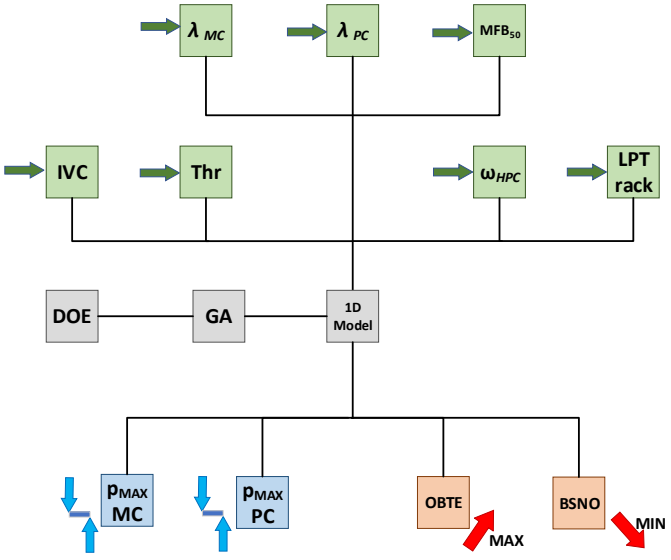

Figure 6. Workflow of the optimization process.

The optimization tool employs a genetic algorithm (MOGA-II), which is the best suited one for a multi-variable multi-objective problem. As said, two objective functions are considered, namely OBTE and BSNO, while seven control variables are varied: throttle valve opening (Thr), target combustion phasing (MFB_{50}), intake valve closure, relative air-fuel ratio in MC and PC, normalized rack position of the LPT and the non-dimensional velocity of E-Comp (ω_{HPC}). The last two parameters vary between 0 and 1. In the case of the LPT, the highest value refers to the maximum opening of the turbine rack, which corresponds to the lowest possible turbine expansion ratio. The second parameter is the E-Comp compressor rotational speed, normalized according to the following expression:

$$\omega_{HPC} = \frac{n_{HPC} - n_{HPC,\min}}{n_{HPC,\max} - n_{HPC,\min}} \quad (4)$$

where n_{HPC} is the actual rotational speed of the E-Comp and the values indexed with "max" and "min" represent the related maximum and minimum levels.

Figure 6 reports the logical scheme of the considered optimization process. The optimizer, at each step of the process, iteratively selects the above control variables, which are passed to the 1D model to perform the numerical analysis. At the end of the simulation, the computed values of the objective functions are passed back to the optimizer for the next iteration, until the optimal levels, belonging to the Pareto Frontier, are obtained. The input parameters of the optimization are varied in the following ranges:

- Thr: 0-90 degrees
- MFB_{50}: 2-9 CAD AFTDC
- IVC: 505-540 CAD AFTDC
- Normalized LPT rack opening: 0-1
- ω_{HPC}: 0-1
- λ_{MC}: 1.5-2.4
- λ_{PC}: 0.8-1.3

Each optimizer evaluation is post-processed to verify that some monitored variables do not exceed the corresponding threshold levels. The same engine operating constraints as the ones specified for the rule-based calibration are applied here.

Assessment between RB and Optimizer Calibrations

The outcomes of the simplified RB calibration methodology are here compared to the optimization outputs (labelled as Opt). The optimization results, shown in the next figures, refer to the solutions which belong to the Pareto Frontier. The OBTE comparison of Figure 7 puts into evidence a quite good agreement all along the BMEP sweep between the considered numerical procedures. A satisfactory RB-Opt agreement is also found for the calibration variables depicted in Figure 8 - Figure 16. Starting the discussion from the mixture qualities in MC and PC, Figure 8 highlights that the maximum OBTE is always reached in the optimization problem with λ_{MC} values close to 2, thus confirming the assumption of the RB calibration. A certain scatter around this optimal value emerges, with a band of ± 0.2. This depends on the complexity of optimization task here considered, consisting in a variable-load, constrained, 7-variable, 2-objective problem. Although more than 5000 iterations have been carried out, the identification of the Pareto Frontier, counting about 650 points, is achieved with a certain scatter band.

A trend against the BMEP appears for the λ_{PC}, shown in Figure 9. In a medium load range (4-13 bar BMEP), a close-to-stoichiometric mixture is preferred, once again with some scatter. For the lower BMEP, a rich λ_{PC} is selected, because of the limitation on the

minimum PC injection duration. At the higher loads, a certain mixture leaning is adopted to limit the PC pressure and temperature peaks, so to reduce the NO production. For some solutions, the maximum allowed injection duration is attained, leading once again to λ_{PC} >1. The MFB_{50} comparison is depicted in Figure 10. Looking to the optimizer outputs, they present an almost flat trend in the medium load range, with most of points at about 8-9 CAD AFTDC. At both higher and lower BMEP values, it is progressively delayed. At high load, this is required to limit the knock, while at low load, it is a consequence of the combustion lengthening and of the constraint on the maximum spark advance. The MFB_{50} derived by the RB calibration presents a similar trend, even if with a slightly earlier MFB_{50} on average.

The results regarding the throttle valve position, plotted in Figure 11, put into evidence that the load is controlled by this device only for BMEP lower than about 5 bar. In these conditions, the throttle valve setting of both RB and Opt strategies are very comparable. The larger scattering of the Opt points for BMEP levels above 5 bar is a consequence of the low load sensitivity to throttle valve openings, when this last is greater than 40-50 degrees. In the same load range, the overall boost is progressively modulated by a partial closure of the LPT rack (Figure 12) and by a simultaneous increase of the E-Comp rotational speed (Figure 13). The overall boosting is shared between the two compressors, according to the pressure ratios plotted in Figure 14 and Figure 15. These figures underlines that, for the optimal calibration, the load is mainly controlled by the LPC, while the E-Comp operates with the minimum possible pressure ratio. This results in a quite relevant exhaust backpressure for the cylinders, but in the minimum possible power request by the E-Comp. In the overall efficiency balance, this calibration strategy proves to be the most effective compared to a calibration which privileges a higher E-Comp boosting.

The last assessment regards the intake valve timing, which is depicted in Figure 16. Generally, a setting close to the most advanced timing is preferred. This choice arises from the opportunity to minimize the pumping losses at low load and control the knock at high load. In the medium BMEP range, the IVC is slightly delayed enhancing the effective volumetric compression ratio and hence the engine thermal efficiency.

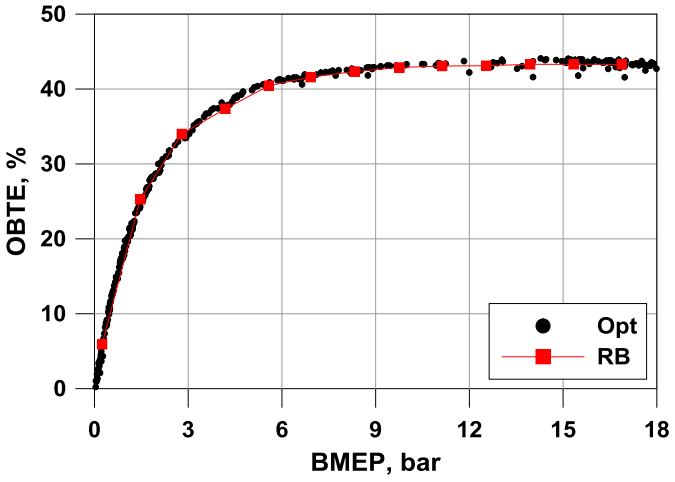

Figure 7. Overall brake thermal efficiency comparison in a BMEP sweep at 3000 rpm for the RB and optimizer calibrations.

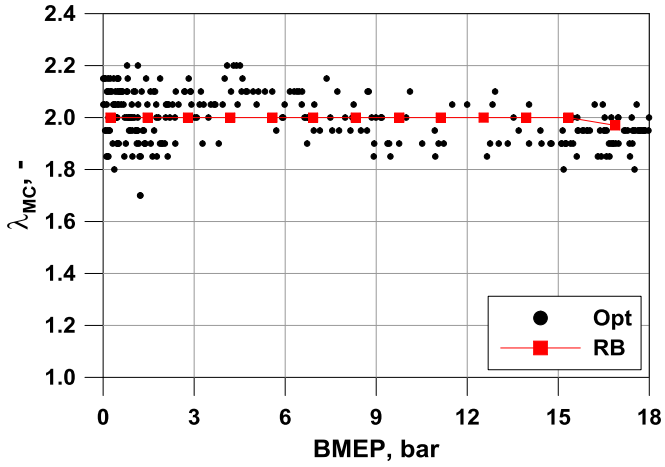

Figure 8. λ_{MC} comparison in a BMEP sweep at 3000 rpm for the RB and optimizer calibrations.

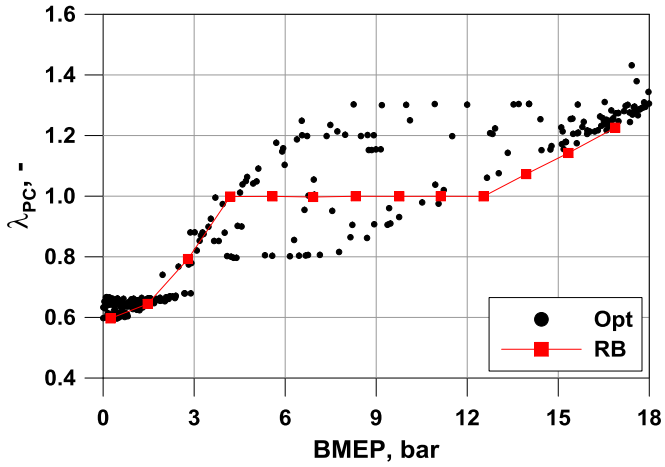

Figure 9. λ_{PC} comparison in a BMEP sweep at 3000 rpm for the RB and optimizer calibrations.

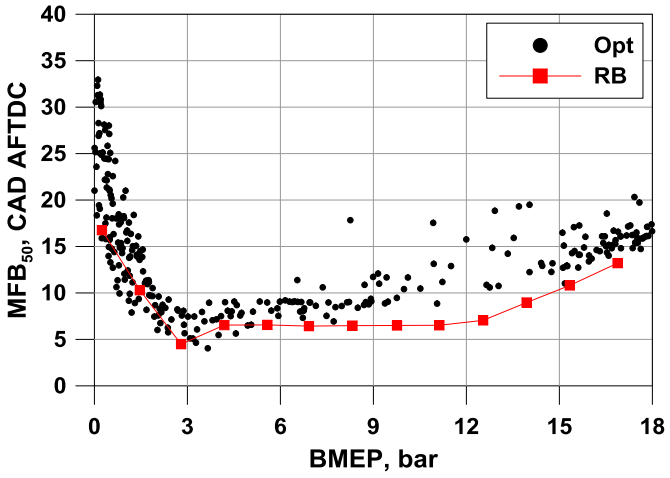

Figure 10. MFB_{50} comparison in a BMEP sweep at 3000 rpm for the RB and optimizer calibrations.

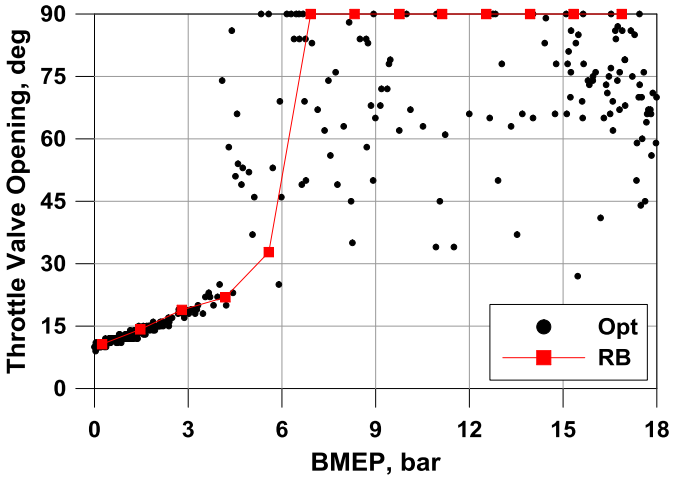

Figure 11. Throttle valve opening comparison in a BMEP sweep at 3000 rpm for the RB and optimizer calibrations.

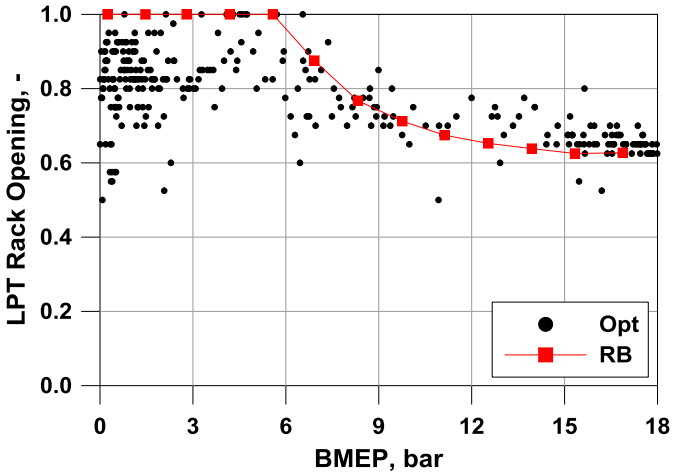

Figure 12. Rack position of LPT comparison in a BMEP sweep at 3000 rpm for the RB and optimizer calibrations.

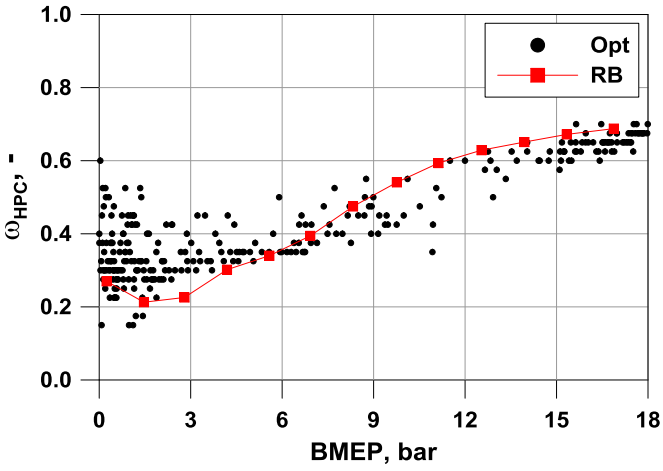

Figure 13. Normalized rotational speed of E-Comp comparison in a BMEP sweep at 3000 rpm for the RB and optimizer calibrations.

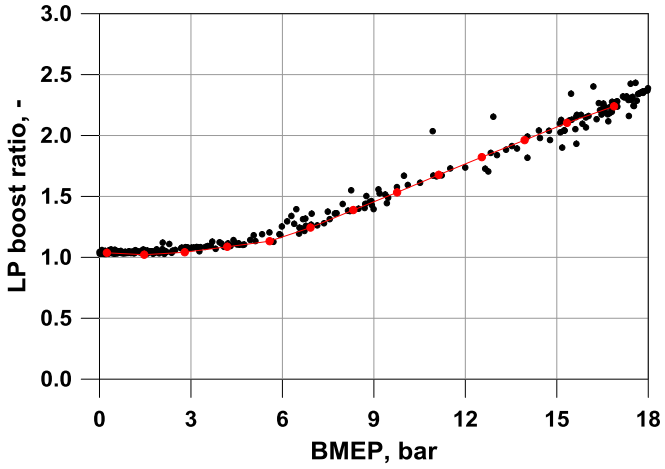

Figure 14. Low Pressure boost ratio comparison in a BMEP sweep at 3000 rpm for the RB and optimizer calibrations.

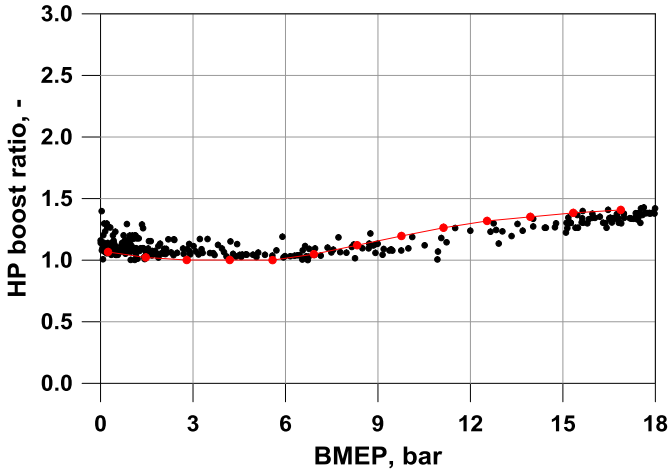

Figure 15. High Pressure boost ratio comparison in a BMEP sweep at 3000 rpm for the RB and optimizer calibrations.

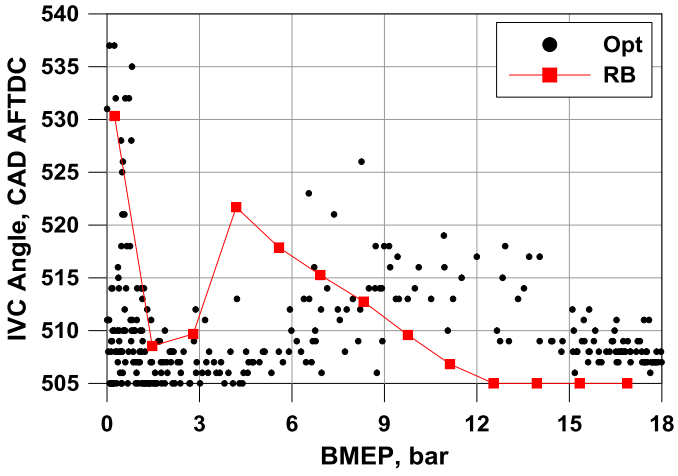

Figure 16. IVC comparison in a BMEP sweep at 3000 rpm for the RB and optimizer calibrations.

As a final remark, the presented results underline that the RB calibration procedure is highly reliable under various load levels, allowing to reach OBTEs very close to the ones derived by the optimizer-based approach. In the light of this observation, the RB

strategy will be extended to the full engine speed range, to explore the close-to-optimal engine performance in the entire operating plane, as discussed in the following section.

Engine Performance Map Discussion

Following the RB control strategy, the whole engine operating plane is computed (composed of 143 operating points - 11 rpm x 13 BMEP). Starting the results discussion from the most important performance parameters, the maps of the standard Brake Thermal Efficiency (BTE) and of the OBTE can be observed in Figure 17 and Figure 18, respectively. In both cases, the maximum levels occur at a medium speed (2500-3500 rpm) and high load (above 12-13 bar BMEP). A peak of BTE (OBTE) of about 46% (43%) is reached, confirming the potential of such engine architecture for a very high efficiency.

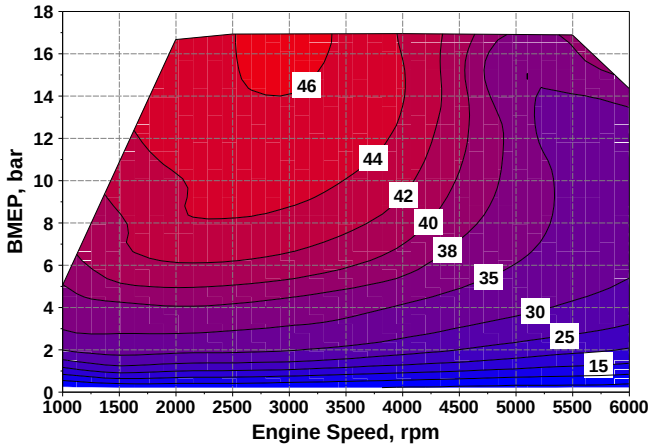

Figure 17. Map of BTE [%].

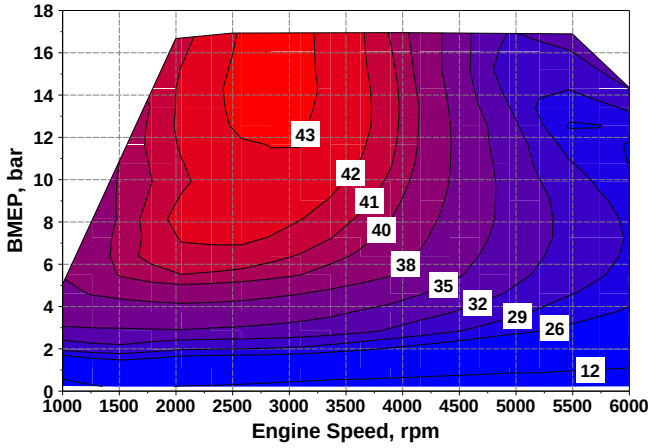

Figure 18. Map of OBTE [%].

The difference between BTE and OBTE is of about 3 percent in this zone, and progressively increases at higher speeds, especially in the high load zone. This is justified by the power absorbed by the E-Comp, whose map is plotted in Figure 19. It can be observed that the compressor requires up to 18 kW, which represents about the 14.3 % of the power rated by the engine. However, the E-Comp power request substantially reduces moving to the map region which is expected to be most frequently experienced by the engine along a WLTP driving cycle, namely close to the maximum efficiency zone. There, the E-Comp power is of about 3 kW.

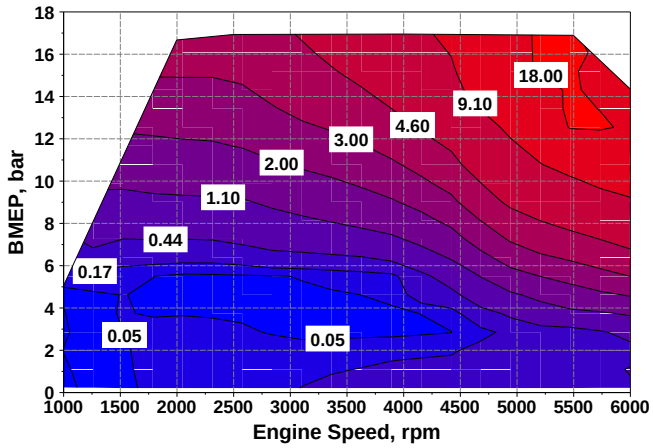

Figure 19. Map of E-Comp power consumption [kW].

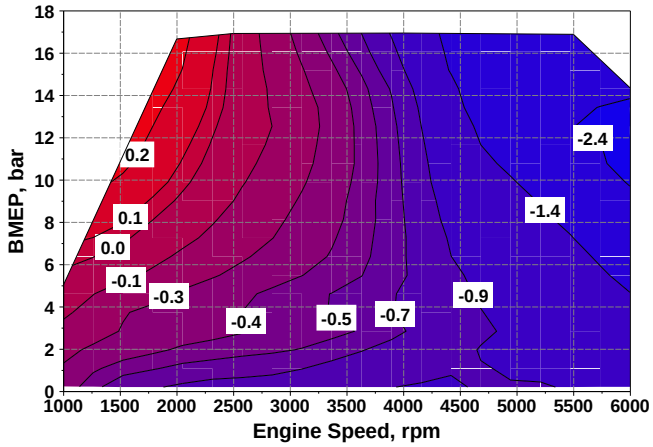

Figure 20. Map of PMEP [bar].

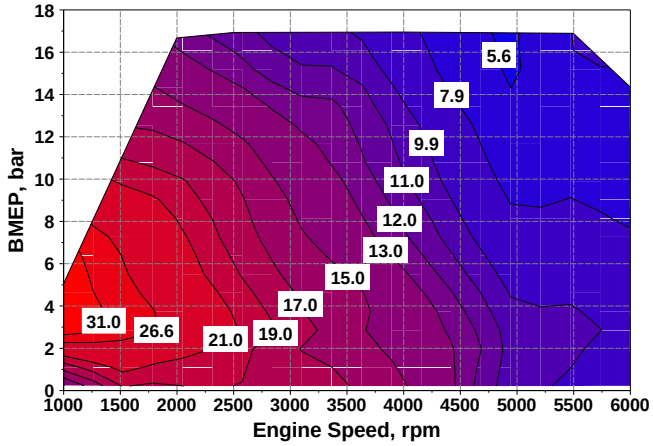

Figure 21. Map of heat losses fraction of total fuel energy [%].

The BTE reduction at increasing speed is mainly due to the pumping losses rising, as shown in Figure 20. Moving down from the full load zone, the efficiency reduction is mainly due to the percent increase of heat losses (Figure 21), which primarily impact at low speeds.

Near to the full load operation, a certain combustion phasing delay is required to limit the knock, as shown in Figure 22, whereas, at medium speeds and loads, a level closer to the MFB_{50} target is

reached. Thanks to the availability of an intake VVT device, a proper Miller strategy is applied. The valve closure is advanced to limit the knock at high BMEP, especially at low speeds (Figure 23). At low load, the same strategy is applied to reduce the intake throttling. In this way, the intake plenum pressure maintains above 1.0 bar in most of the map (Figure 24), and above 0.5 bar even in the region at very low BMEP. To fulfill the load target with an ultra-lean air/fuel mixture and a Miller strategy, a very high plenum pressure is required, with peaks of 3.8 bar at the highest speeds and loads.

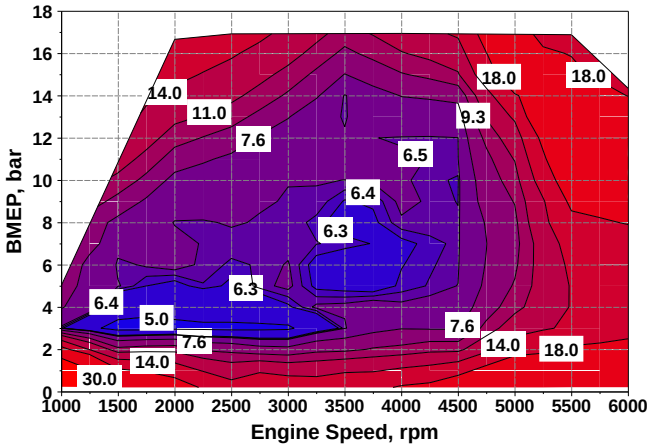

Figure 22. Map of MFB_{50} for the main chamber [CAD AFTDC].

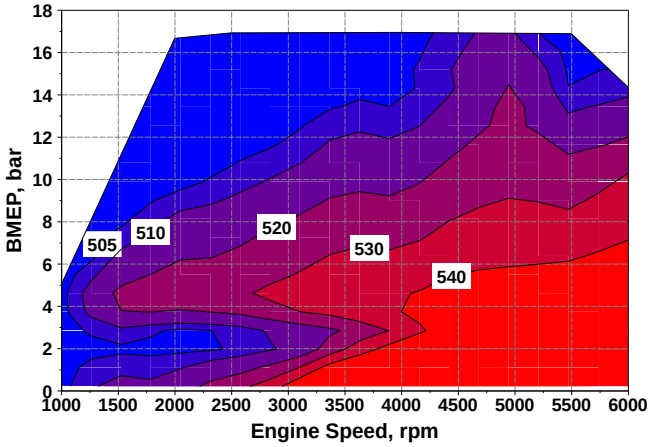

Figure 23. Map of the IVC [CAD AFTDC].

The combustion process is highly affected by the operating conditions, as shown in Figure 25, which depicts the combustion duration $MFB_{10\text{-}90}$. An adequate combustion speed occurs over the whole plane, despite the considered ultra-lean operation. Indeed, the $MFB_{10\text{-}90}$ maintains below 48 CADs at the higher speeds, while at the lower speeds and mid/high loads, it reduces even down to 9 CADs. At very low loads, a combustion lengthening can be observed, which reflects on the MFB_{50} delay (Figure 22). The predicted specific emissions of CO, NO and HC are plotted in Figure 26, Figure 27 and Figure 28, respectively. CO and NO data are very low over the whole engine plane thanks to the ultra-lean mixture. This limits the temperature peaks in the burned zone, inhibiting the formation of the above pollutants. NO specific emissions present a certain increase only in the operating conditions where a rich λ_{PC} is assigned (see Figure 29). This is a consequence of the limitation on the minimum injection duration. For the considered engine, NO production concentrates in the pre-chamber, because of the higher burned temperature compared to the one in the main-chamber. Despite the strong excess-air, HC emissions are not negligible over the whole engine plane. This is once again due to the reduced in-cylinder temperatures which inhibits post-oxidation compared to a conventional engine. The brake specific HC increases at reducing speed and load mainly because of the decreasing thermal efficiency.

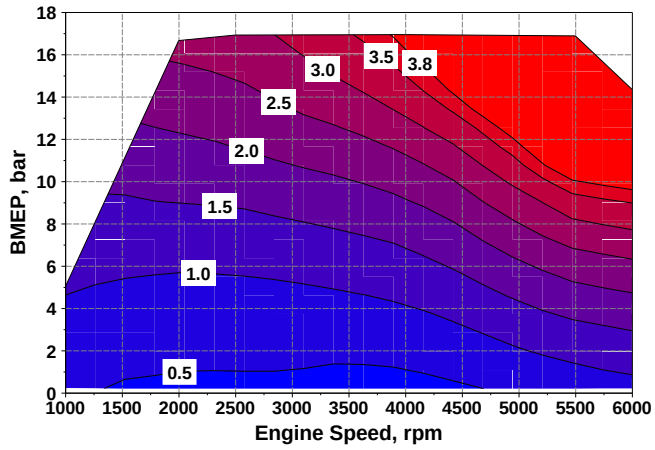

Figure 24. Map of intake plenum pressure [bar].

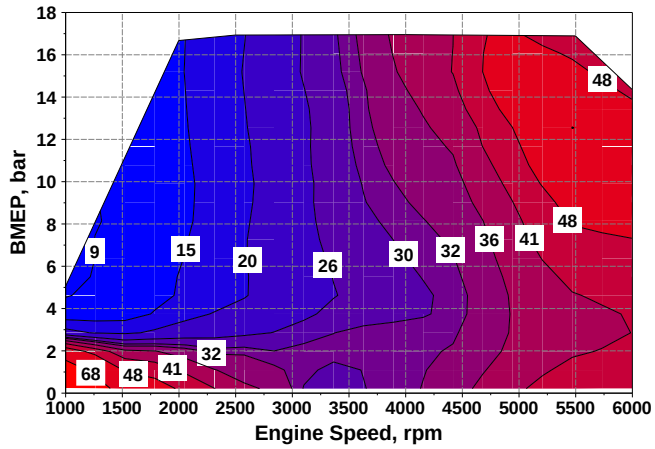

Figure 25. Map of $MFB_{10\text{-}90}$ [CAD].

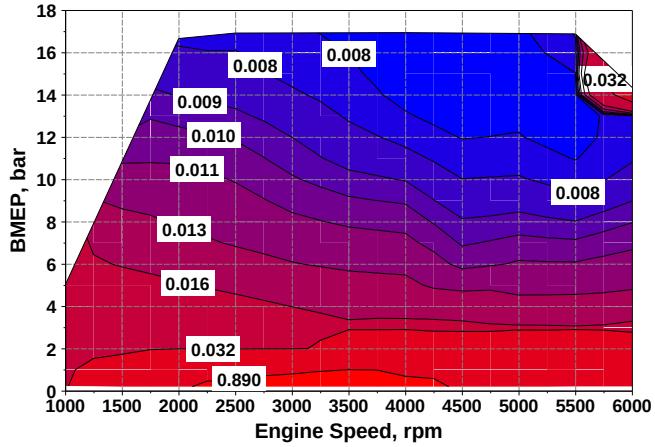

Figure 26. Map of brake specific CO emission [g/kWh].

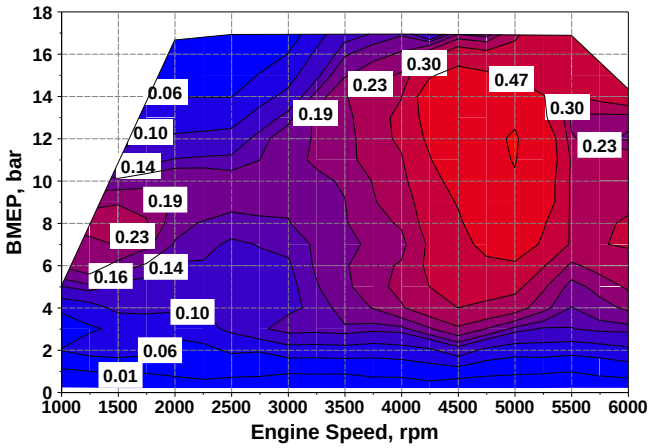

Figure 27. Map of brake specific NO emission [g/kWh].

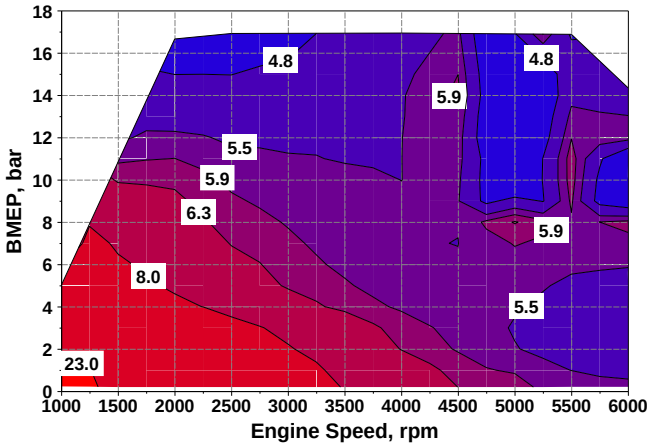

Figure 28. Map of brake specific HC emission [g/kWh].

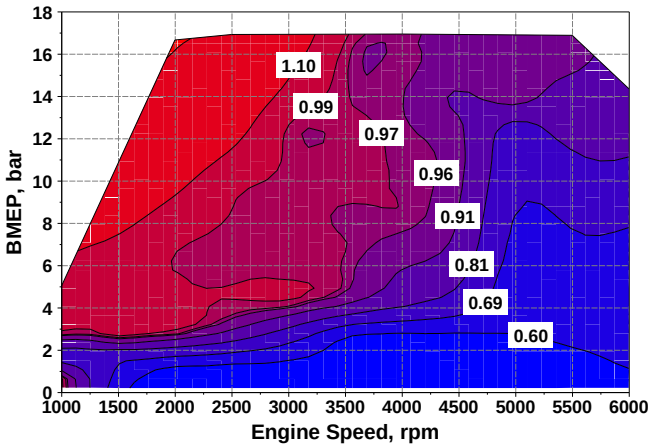

Figure 29. Map of λ_{PC} [-].

Conclusions

In the present work, the performance and emissions of an advanced multi-cylinder "ultra-lean" pre-chamber SI engine are numerically investigated. The study is based on a 1D engine model. The simulation is enhanced with refined sub-models of turbulence, combustion, heat transfer and knock. These sub-models are widely validated in previous authors' works.

A rule-based calibration procedure is proposed and implemented in a single control block in the adopted 1D code. It allows to compute the performance maps and to identify the close-to-optimal control variables, aiming to reach a compromise between maximum overall brake thermal efficiency and minimum brake specific nitric oxides. The above methodology is verified against the outcomes of a more complex calibration approach, implemented in an external optimizer based on a genetic algorithm. The assessment between the calibration methodologies, along a load sweep at a constant speed of 3000 rpm, demonstrates the reliability of the simplified rule-based calibration procedure. Subsequently, the RB approach is used to compute some performance/calibration parameters and emissions over the whole engine operating plane.

The analysis of the computed maps shows that the engine reaches the maximum levels of OBTE at medium speed and high load (up to 43%), due to the positive superimposition of various effects such as efficient combustion even under ultra-lean mixture condition (λ_{MC} = 2 in most operating points), reduced pumping and heat losses, and acceptable power absorbed by the E-Comp. Such benefits remain over a large portion of the operating plane. At high speeds, the main drawbacks are the increased pumping losses and the E-Comp power request. Knocking combustions are avoided by a combination of Miller intake strategy and combustion phasing delay. The Miller strategy also helps to reduce the intake throttling at low BMEP. The calibration strategy for the two-stage boosting system involves the highest contribution to engine boosting from LP compressor, with a certain penalization of the exhaust backpressure. The predicted NO and CO emissions are reduced due to the ultra-lean mixture, while quite significant HC emissions emerge, which mainly derive from low temperature during the expansion phase.

Summarizing, the developed calibration procedure shows the potentials to predict, on a physical basis, the overall performance and the exhaust emissions in the whole engine operating plane. The proposed methodology represents an effective tool capable to forecast the behavior of a complex engine architecture, contributing to support and drive the discussed high-efficiency engine development phase.

References

1. Ntziachristos, L., Mellios, G., Samaras, Z., "What is the real-world CO_2 reduction benefit of the 95 g/km passenger car average emission target to be reached by 2020?", *Procedia-Social and Behavioral Sciences 48*: 2048-2057, 2012, doi:10.1016/j.sbspro.2012.06.1178.
2. Fontaras, G., Zacharof, N., Ciuffo, B., "Fuel consumption and CO_2 emissions from passenger cars in Europe–Laboratory versus real-world emissions." *Progress in Energy and Combustion Science* 60:97-131, 2017, doi:10.1016/j.pecs.2016.12.004.
3. Sperling, D., "Future drive: Electric vehicles and sustainable transportation," (Island Press, 2013), ISBN: 9781559633277.
4. Saber, A., Venayagamoorthy, G., "Plug-in vehicles and renewable energy sources for cost and emission reductions," *IEEE Transactions on Industrial electronics* 58.4 1229-1238,2011, doi:10.1109/TIE.2010.2047828.
5. Khaligh, A., Li, Z., "Battery, ultracapacitor, fuel cell, and hybrid energy storage systems for electric, hybrid electric, fuel cell, and plug-in hybrid electric vehicles: State of the art," *IEEE transactions on Vehicular Technology*, *59*(6), 2806-2814, 2010, doi:10.1109/TVT.2010.2047877.

6. European Environment Agency, "Annual European Union greenhouse gas inventory 1990–2016 and inventory report 2018," Report No.:5/2018, 2018.
7. Shaik, A., Moorthi, N., Rudramoorthy, R., "Variable Compression ratio engine: a future power plant for automobiles-an overview", *Proc. of the Istitution of Mechanical Engineers Part D: Journal of Aut. Eng.* 221(9):1159-1168, 2007, doi: 10.1243:09544070JAUTO573.
8. Bozza, F., De Bellis, V., Teodosio, L., Tufano, D., et al., "Techniques for CO_2 Emission Reduction over a WLTC. A Numerical Comparison of Increased Compression Ratio, Cooled EGR and Water Injection," SAE Technical Paper 2018-37-0008, 2018, doi:10.4271/2018-37-0008.
9. Germane, G., Wood, C., Hess, C., "Lean Combustion in Spark-Ignited Internal Combustion Engines - A Review," SAE Technical Paper 831694, 1983, doi:10.4271/831694.
10. Rapp, V., Killingsworth, N., Therkelsen, P., et al., "Lean Combustion, 2nd Edition," Lean-Burn Internal Combustion Engines, Elsevier, 2016, 111-146, doi:10.1016/C2013-0-13446-0.
11. Quader, A., "Lean combustion and the misfire limit in spark ignition engines," SAE Technical Paper 741055, 1974, doi:10.4271/741055.
12. Heywood, J., "*Internal combustion engine fundamentals*," Vol. 930 (New York, Mcgraw-Hill, 1988), ISBN: 007028637X.
13. Toulson, E., Schock, H., Attard, W., "A Review of Pre-Chamber Initiated Jet Ignition Combustion Systems," SAE Technical Paper 2010-01-2263, 2010, doi:10.4271/2010-01-2263.
14. Sens, M., Binder, E., "Pre-Chamber Ignition as a Key Technology for Future Powertrain Fleets," MTZ worldwide, 80(2), 44-51, 2019, doi:10.1007/s38313-018-0150-1.
15. Mueller, C., Morcinkowski, B., Schernus, C., Habermann, K., Uhlmann, T., "Development of a pre-chamber for spark ignition engines in vehicle applications," 4th International Conference on Ignition Systems for Gasoline Engines, Dec. 2018, doi: 10.5445/IR/1000088588.
16. Shapiro, E., Tiney, N., Kyrtatos, P., Kotzagianni, M., et al., "Experimental and Numerical Analysis of Pre-Chamber Combustion Systems for Lean Burn Gas Engines" SAE Technical Paper No. 2019-01-0260, 2019, doi:10.4271/2019-01-0260.
17. Bureshaid, K., Feng, D., Zhao, H., Bunce, M., "Combustion and emissions of gasoline, anhydrous ethanol, and wet ethanol in an optical engine with a turbulent jet ignition system," *Proceedings of the Institution of Mechanical Engineers, Part D: Journal of Automobile Engineering*, 2019, doi:10.1177/0954407019825999.
18. Lumsden, G., Watson, H., "Optimum Control of an S.I. Engine with a λ=5 Capability," SAE Technical Paper 950689, 1995, doi:10.4271/950689.
19. Schumacher, M., Wensing, M., "A Gasoline Fuelled Pre-Chamber Ignition System for Homogeneous Lean Combustion Processes," SAE Technical Paper 2016-01-2176, 2016, doi:10.4271/2016-01-2176.
20. Adomeit, P., Glück, S., Sehr, A. and Wedowswski, S., "Two-stage turbocharging-concept for high pressure charging on SI-engines," *MTZ worldwide*, 201071(5), pp.50-54, doi:10.1007/BF03227016 2010.
21. Bozza, F., De Bellis, V., Tufano, D., Malfi, E. et al., "A Quasi-Dimensional Model of Pre-Chamber Spark-Ignition Engines," SAE Technical Paper 2019-01-0470, 2019, doi:10.4271/2019-01-0470.
22. Gottschalk, W., Lezius, U., Mathusall, L., "Investigations on the Potential of a Variable Miller Cycle for SI Knock Control" SAE Technical Paper 2013-01-1122, 2013, doi: 10.4271/2013-01-1122.
23. De Bellis, V., Severi, E., Fontanesi, S., Bozza, F., "Hierarchical 1D/3D approach for the development of a turbulent combustion model applied to a VVA turbocharged engine. Part II: Combustion model", *Energy Procedia* 45: 1027-1036, 2014, doi: 10.1016/j.egypro.2014.01.108.
24. Gatowsky, J., Heywood, J., "Flame Photographs in a Spark-Ignition Engine", *Combustion and Flame* 56:71-81, 1984, doi:10.1016/0010-2180(84)90006-3.
25. Hiraoka, K., Nomura, K., Yuuki, A., Oda, Y. et al., "Phenomenological 0-Dimensional Combustion Model for Spark-Ignition Natural Gas Engine Equipped with Pre-Chamber," SAE Technical Paper 2016-01-0556, 2016, doi: 10.4271/2016-01-0556.
26. Bounaceur, R., Herbinet, O., Fournet, R., Glaude, P. et al., "Modeling the Laminar Flame Speed of Natural Gas and Gasoline Surrogates," SAE Technical Paper 2010-01-0546, 2010, doi: 10.4271/2010-01-0546.
27. Bozza, F., Teodosio, L., De Bellis, V., Fontanesi, S. et al., "A Refined 0D Turbulence Model to Predict Tumble and Turbulence in SI Engines," *SAE Int. J. Engines* 12(1):15-30, 2019, doi:10.4271/03-12-01-0002.
28. Bozza, F., De Bellis, V., Teodosio, L., "A Tabulated-Chemistry Approach Applied to a Quasi-Dimensional Combustion Model for a Fast and Accurate Knock Prediction in Spark-Ignition Engines," SAE Technical Paper 2019-01-0471, 2019, doi:10.4271/2019-01-0471.
29. Lavoie, G., Heywood, J., Keck, J., "Experimental and theoretical study of nitric oxide formation in internal combustion engines" *Combustion science and technology*, 1(4): 313–326, 1970, doi:10.1080/00102206908952211.
30. Kaplan, J. , Heywood, J., "Modeling the spark ignition engine warm-up process to predict component temperatures and hydrocarbon emissions", SAE Technical Paper 1991, 361-376, doi:10.4271/910302.
31. Lavoie, G., "Correlations of combustion data for SI Engine calculations–laminar flame speed, quench distance and global reaction rates," SAE Technical Paper1978,1015-1033, doi: 10.4271/780229.
32. Schramm, J., Sorenson, S., "A model for hydrocarbon emissions from SI engines," SAE Technical Paper 1990, 2331-2349, doi: 10.4271/902169.
33. Serrano, D., Zaccardi, J., Libert, C., Müller, C., Habermann,K., "Ultra-Lean Pre-Chamber Gasoline Engine for Future Hybrid Powertrains,"19ICENA-0206, 2019.
34. Bozza, F., De Bellis, V., Teodosio, L., "A numerical procedure for the calibration of a turbocharged spark-ignition variable valve actuation engine at part load", *Int. J. of Engine Research* 18(8), 810-823, 2016. doi:10.1177/1468087416674653.

Acknowledgements

"This project has received funding from the European Union's Horizon 2020 research and innovation programme under grant agreement No 724084"

Contact information

F. Bozza, Full Professor, (fabio.bozza@unina.it),
D. Tufano, PhD Student, (daniela.tufano@unina.it),
E. Malfi, PhD Student, (enrica.malfi@unina.it),
L. Teodosio, Research Fellow, (luigi.teodosio@unina.it),
V. De Bellis, Researcher, (vincenzo.debellis@unina.it)
University of Naples "Federico II", Naples, Italy, +39-081-7683274.
C. Libert, Project Leader (cedric.libert@renault.com)
Renault-Nissan-Mitsubishi

Acronyms

0D-1D-3D	Zero-One-Three-dimensional
AFTDC	After firing top dead center
AI	Auto-ignition
Ba	Battery
BB	Base boost
BMEP	Brake mean effective pressure
BSNO	Brake specific nitrogen oxide
BTE	Brake thermal efficiency
CAD	Crank angle degree
CFD	Computational fluid dynamics
E-Comp	Electrical compressor
EG	Electric generator
EGR	Exhaust gas recirculation
EM	Electric motor
FL	Full load
HEV	Hybrid electric vehicle
HP	High pressure
ICE	Internal combustion engine
IVC	Intake valve closing
LHV	Low heating value
LP	Low pressure
LPC	Low-pressure compressor
LPT	Low-pressure turbine
MC	Main-chamber
MFB	Mass fraction burned
OBTE	Optimal brake thermal efficiency
PC	Pre-chamber
PID	Proportional integral derivative
RB	Rule-based
SA	Spark advance
SI	Spark ignition
Thr	Throttle
TRF	Toluene reference fuel
VVT	Variable valve timing
WLTC	Worldwide harmonized Light vehicles Test Cycles

Symbols

A_L	Laminar flame area
A_T	Turbulent flame area
D_3	Fractal dimension
Inj	Injector
k	Turbulent kinetic energy
K	Mean flow kinetic energy
L_{min}, L_{max}	Minimum / maximum flame front wrinkling scale
$\dot{m}_f$	Fuel flow rate
n	Rotational speed
P_{HPC}	Power absorbed by the E-Comp
P_{ICE}	Engine brake power
S_L	Laminar flame speed
T	Tumble angular momentum
u'	Turbulence intensity

Greeks

τ_{AI}	Auto ignition time
η	Efficiency
λ	Relative air/fuel ratio
ρ	Gas density
ω	Normalized rotational speed

Subscripts

10 / 50 / 90	Referring to 10 / 50 / 90% of mass fraction burned
u	Unburned